Reductive Oligomerization of Nitroaniline Catalyzed by Fe_3O_4 Spheres Decorated with Group 11 Metal Nanoparticles

Carlos Alberto Huerta-Aguilar,* Rajendra Srivastava, Jesús A. Arenas-Alatorre, and Pandiyan Thangarasu*

ACCESS | 📊 Metrics & More | 📖 Article Recommendations | 🔷 Supporting Information

ABSTRACT: The present work demonstrates a simple and sustainable method for forming azo oligomers from low-value compounds such as nitroaniline. The reductive oligomerization of 4-nitroaniline was achieved via azo bonding using nanometric Fe_3O_4 spheres doped with metallic nanoparticles (Cu NPs, Ag NPs, and Au NPs), which were characterized by different analytical methods. The magnetic saturation (M_s) of the samples showed that they are magnetically recoverable from aqueous environments. The effective reduction of nitroaniline followed pseudo-first-order kinetics, reaching a maximum conversion of about 97%. Fe_3O_4-Au is the best catalyst, its a reaction rate ($k_{Fe_3O_4\text{-}Au} = 0.416$ mM L^{-1} min^{-1}) is about 20 times higher than that of bare Fe_3O_4 ($k_{Fe_3O_4} = 0.018$ mM L^{-1} min^{-1}). The formation of the two main products was determined by high-performance liquid chromatography-mass spectrometry (HPLC-MS), evidencing the effective oligomerization of NA through N = N azo linkage. It is consistent with the total carbon balance and the structural analysis by density functional theory (DFT)-based total energy. The first product, a six-unit azo oligomer, was formed at the beginning of the reaction through a shorter, two-unit molecule. The nitroaniline reduction is controllable and thermodynamically viable, as shown in the computational studies.
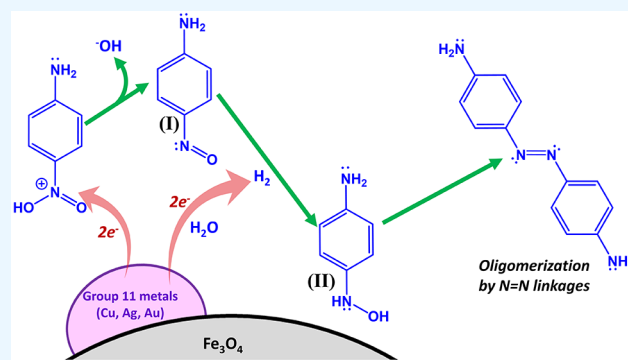
INTRODUCTION

Anilines and aromatic azo molecules are industrially produced by catalytic reduction of toxic nitrobenzene at high temperature and pressure[1] and it is known that aromatic azo polymers are common precursors in the synthetic organic industry.[2] However, aromatic imine production is essential for the modern industry; thus, the search for alternative less toxic methods is the topic of interest for the above production. But the reaction mechanism of the reduction of nitrobenzene is complicated as it depends on several parameters such as solvent, temperature, size, and composition of the catalyst although the Haber type of reaction mechanism is the most accepted one.[3] The environmental production agency is regularly monitoring the industrial process and evaluating the environmental impact from the industrial hazardous waste.[4] So, a standardized method is required for the reduction of nitroaniline, where the catalytic material plays a vital role in the large-scale production since the industrial reductive process is expensive because of poor selectivity in the purification process.[5] Even though costly metals such as platinum[6] and gold[7] have been widely employed as catalysts for the reduction of organic compounds due to their stability and high efficiencies[8] over other low-cost transition metals (TM) such as Cu,[9] Ni,[10] and Ru,[11] the latter have started being used lately

as catalysts for the organic reactions to cut the cost. The metal-based micro- or nano-sized powders are considered as potential industrial catalysts because of their exponentially greater active sites (surface area to volume ratio) caused by quantum confinement effects.[12] It has been reported that nanometric catalysts have enhanced stereo- and enantio-selectivity to improve the efficiency of the reactions.[13] To improve further the performance of the catalyst, it is common to mix multiple metals[14] to yield hybrid organic/inorganic materials such as Pd/C,[15] Pt/C, and Pd/graphene.[16]

Metal oxides are also good candidates for catalysts, especially, iron oxides, which are cheap, robust, nontoxic, eco-friendly, easy to handle, and magnetically separable for reuse. They are actively considered from the environmental point of view[17] since iron can be easily removed in biological reactions[18] as compared to other metallic or chalcogen
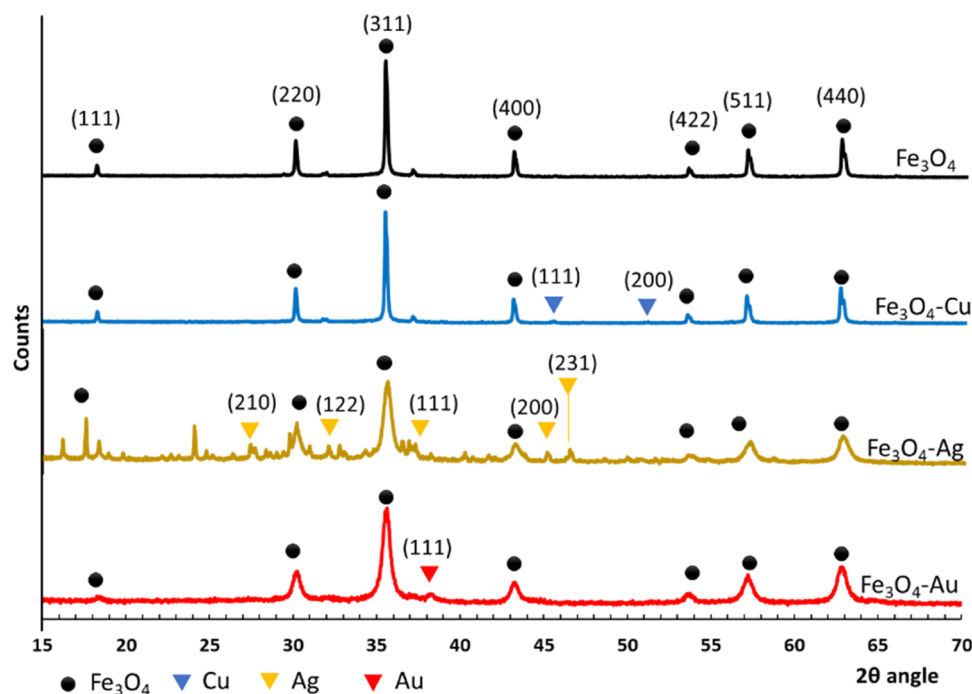
Figure 1. XRD patterns of magnetite-based samples.

oxides.[19] Fe_3O_4 (magnetite) can be used for H_2/hydrogenation if it is mixed with Ni,[20] and can be employed for organic reduction in the presence of CO and H_2O.[21] Magnetite is presented in the stoichiometric ratio of 1:1 (FeO/Fe_2O_3) and 1:2 (Fe^{2+}/Fe^{3+}) in a closed cubic lattice. Typically, Fe^{2+} is positioned at tetrahedral sites whereas Fe^{3+} occupies octahedral sites within the crystal structure. The understanding of the exact stoichiometry of Fe_3O_4 is limited, but the superparamagnetic and catalytic properties of the sample can be maintained without a significant change in the structure ($Fe_{3-\delta}O_4$) $Fe_{3-\delta}O_4$.[22] Fe_3O_4, a narrow-band gap energy semiconductor, has a property of visible light-harvesting character. However, the recombination effect of e^-/h^+ is very high; thus, the addition of metals to Fe_3O_4 can reduce the recombination effect of e^-/h^+, decreasing the band gap energy.[23] This means that the valence band (VB)−conduction band (CB) interband states can be modified by employing the metal work function;[24] as a result, the Fe_3O_4−metal conjugation exhibits a greater photostability and higher extinction coefficients, improving the catalytical, physical, and chemical properties.[25] So, the present work is focused on the deposition of Au NPs, Ag NPs, and Cu NPs on Fe_3O_4 and analyzes the impact of electronic and magnetic properties on the catalytic reduction of 4-nitroaniline. The formation of oligomers was optimized and the total energy determined by the density functional theory was analyzed for each product formed in the reduction, which is interesting and, to the best of our knowledge, has not been reported in the literature. One-step, recoverable, and reusable catalytic systems such as Fe_3O_4-M (M = Cu, Ag, and Au) are prepared and characterized completely, and employed for the selective reduction of 4-nitroaniline (NA) at room conditions.

■ RESULTS AND DISCUSSION

Characterizations. *X-ray Diffraction (XRD).* The characteristic XRD peaks of Fe_3O_4 planes are observed in all samples at 2θ = 18.0 [111], 30.1 [220], 34.8 [311], 43.7 [400], 53.2

[422], 56.8 [511], and 59.5 [400] corresponding to JCPDS 19-0629.[26] The average grain size of the samples calculated by Scherrer's equation was around 10.69 nm.[27] Fe_3O_4-Cu corresponds to cubic Cu clusters and it is identified at 2θ = 46.5 [111] and 52 [200], coinciding with JCPDF 04-0836.[28] For Fe_3O_4-Ag, there is a typical *fcc*-Ag pattern at 2θ = 27.8 [210], 32.2 [122], 38.1 [111], and 44.3 [200] (JCPDS No. 04-0783)[29] despite having a secondary phase characterized as sodium carbonate, which was used to reduce Ag^+ to Ag NPs (JCPDS 37-0451).[30] Similarly, for Fe_3O_4-Au, the presence of *fcc* phase was seen as the signal was detected at 2θ = 37.8 [111] as reported with JCPDS No. 04-0784,[31] for which, particularly, a broadening of the peaks was observed due to a lack of periodicity in the small particles (Figure 1).

Scanning Electron Microscopy (SEM). After analyzing the SEM micrographs (Figure 2), which reveal the existence of uniform spherical particles (∼75 nm),[32] for example, the deposition of Ag and Au NPs on Fe_3O_4 exhibits the presence of small bright dots, showing dense aggregations uniformly dispersed over massive Fe_3O_4 particles (Figure 2c,d), while for Fe_3O_4-Cu, since the difference of size and mass between Fe and Cu is almost similar, it averts direct identification of Cu nanostructures.[33]

Transmission electron microscopy (TEM) studies were performed for the samples (Figure 3), showing that Fe_3O_4 NPs are presented in semispherical form with the size of 70−80 nm. This observation is seen to be consistent with other samples, and also seen are small dense particles over the surface of iron oxide spheres; for Fe_3O_4-Cu, the particle size was around 20 nm (Figure 3a); for Fe_3O_4-Ag and Fe_3O_4-Au, it was 17−30 nm (Ag black dense particle), and for Ag NPs, 10−30 nm.

Energy Dispersive X-ray Spectroscopy (EDS). The elemental composition of the samples (Table S1) shows that in all of the samples, the contents of Fe and O are close to the theoretical values derived for Fe_3O_4 (O = 27.64%, 57.15% atom; Fe = 72.36% Elem., 42.85% atom).[34] The metal deposition in all of the samples was less than 1.0% and the
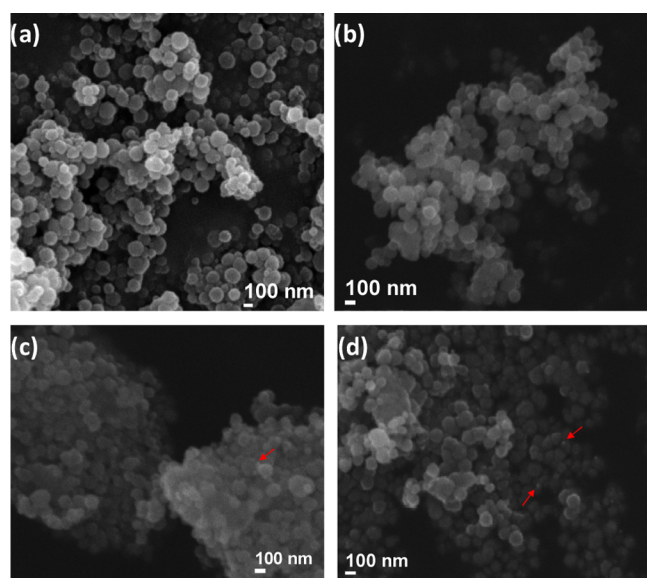
Figure 2. SEM analysis of magnetite nanoparticles: (a) bare Fe_3O_4; (b) Fe_3O_4-Cu; (c) Fe_3O_4-Ag; and (d) Fe_3O_4-Au.

scattering of these NPs over the large magnetite surface was as follows: Cu = 0.52%, 0.30% atom; Ag = 0.83% Elem., 0.77% atom; and Au = 0.53% Elem., 0.52% atom. The EDS spectrum in Figure S1 shows peaks of Fe ($K\alpha$ = 6.40 keV and $L\alpha$ = 0.70 keV) and O ($K\alpha$ = 0.52 keV); in Fe_3O_4-Cu, Cu $K\alpha$ is found at E = 8.0 keV; in Fe_3O_4-Ag, Ag $K\alpha$ at E = 2.98 keV; and for Fe_3O_4-Au, the peak at 10 keV was assigned to Au $K\alpha$.[35] In all samples, a trace of chlorine was found, possibly, from the water.

X-ray Photoelectron Spectroscopy (XPS). The oxidation state of the metal ion was studied by XPS (Figure S2), showing that in all of the samples (Fe_3O_4-Cu, Fe_3O_4-Ag, and Fe_3O_4-Au), the presence of Fe_3O_4 is established as a main component. There is also an Na residual (Na 1s, E_B = 1085.2 eV) originated from sodium acetate and carbonate, which were used in the sample preparation; besides, there is a carbon C 1s signal at E_B = 284 eV due to organic residual and chamber contamination. A typical OKLL is found between E_B = 970 and 986 eV for the samples. The presence of Fe^{3+} is confirmed by observing the peaks Fe $2p_{3/2}$ = 710 ± 0.39 eV and Fe $2p_{1/2}$ = 724 ± 0.26 eV, which establishes the existence of magnetite due to the lack of the satellite peak (Figure S3) and is commonly found in other Fe^{3+} oxides.[36] The additional Fe 3p signal observed is attributed to the iron present in the high-spin Fe^{2+} and Fe^{3+},[37] as seen at 53.43 ± 0.37 eV (Table S2). After observing the O1s signal, which gives a good insight into the structures,[38] the presence of surface-adsorbed water

and hydroxyl groups is recognized at 531.5 ± 0.46 eV as the split signals in 528−532 eV, and the peaks at 528.4 ± 0.34 eV are contributed from the lattice oxygen species (O_2^-).[39] The surface deposition of Group 11 metal NPs (Fe_3O_4-Cu, Fe_3O_4-Ag, and Fe_3O_4-Au) is confirmed by XPS and the peaks corresponding to Cu ($2p_{3/2}$ = 931.81 eV and $2p_{1/2}$ = 953.63 eV) are observed; nevertheless, the appearance of a satellite at E_B = 942.5 eV is the footprint of Cu^{2+} and it is a natural tendency of Cu^0 when it gets oxidized under room conditions. For Fe_3O_4-Ag, the signals $3d_{5/2}$ = 366.03 eV and Ag $3d_{3/2}$ = 372.27 eV were seen, showing the presence of Ag.[40] Finally, for Fe_3O_4-Au, 4f corresponding to gold was detected at 91.44 eV[41] and the signal was still detectable despite the interference of Fe 3s.

Magnetic Properties. The hysteresis curves for Fe_3O_4-Cu, Fe_3O_4-Ag, and Fe_3O_4-Au were obtained using the vibrating sample magnetometer (VSM) by applying the external magnetic fields at 298 and 5.0 K, and it revealed magnetic saturation (M_s) for bare Fe_3O_4, Fe_3O_4-Cu, Fe_3O_4-Ag, and Fe_3O_4-Au. The M_s values are almost similar without a significant change (56.8 and 59.9 emu/g); however, for Fe_3O_4-Ag, the magnetization reached to 75.5 emu/g since M_s is directly related to the nature of metals deposited on the magnetite surface (Figure 4).[42] The hysteresis loops suggest the presence of single-domain grains contributing to super-paramagnetic behavior.[43]
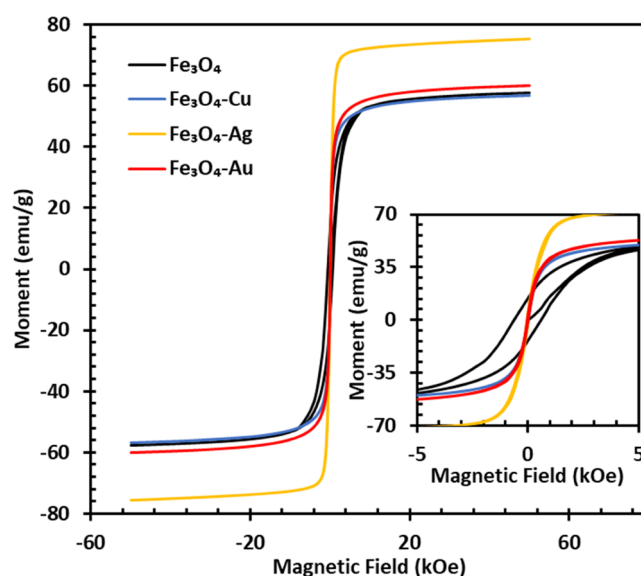
Figure 4. Magnetic hysteresis loops of Fe_3O_4, Fe_3O_4-Cu, Fe_3O_4-Ag, and Fe_3O_4-Au.
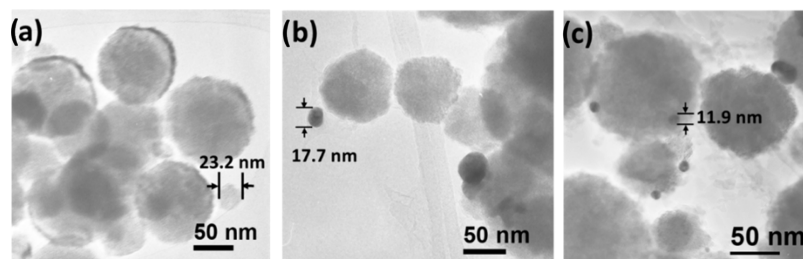
Figure 3. TEM images of the samples: (a) Fe_3O_4-Cu; (b) Fe_3O_4-Ag; and (c) Fe_3O_4-Au.
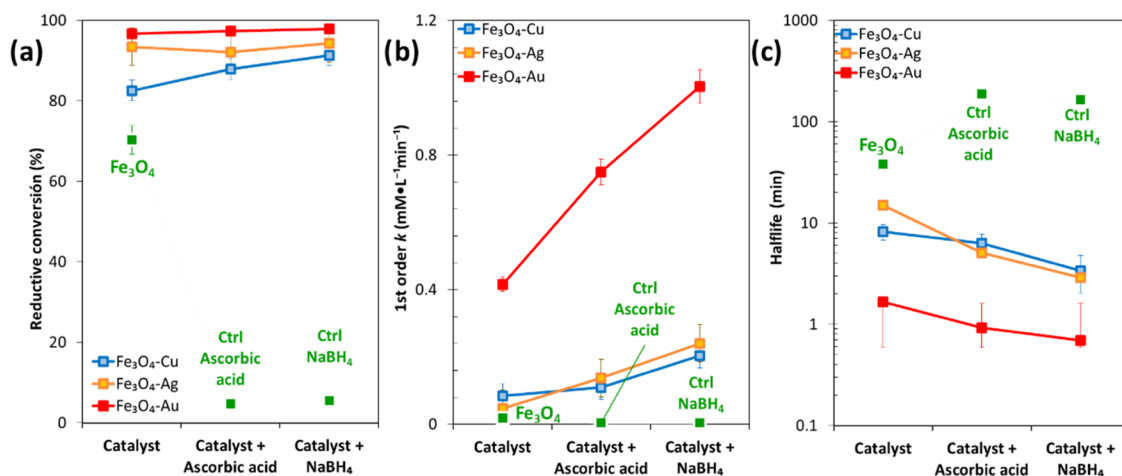
Figure 5. Reduction of 4-nitroaniline by magnetite catalysts (Fe_3O_4, Fe_3O_4-Cu, Fe_3O_4-Ag, and Fe_3O_4-Au): (a) reduction yield and (b) first-order kinetics; (c) half-life of the conversion of NA to oligomers under the catalytic process.

Group 11 metals have $ns^1(n-1)d^{10}$ valence electrons acting as e^- scavengers and they increase the response of the materials toward external magnetic fields.[44] In Fe_3O_4-Cu, this effect is debilitated due to the small size of Cu atoms as a higher M_s is anticipated if the size of the atom is increased; nevertheless, in the case of Au, the distortion in crystal lattices is expected by the crystal defects and it is directly related to the reduction of the magnetic moment inside particles because of the magnetocrystalline anisotropy effect.[45] In particular, for Fe_3O_4-Ag, the Ag electron scavenger effect could affect the magnetic response while its smaller atom size will not cause strong distortions in the magnetite particle's surface; thus, it exhibits superparamagnetic property, so, these types of samples can be efficiently recovered after the catalysis.[46] The squareness ratio (SQ), defined as M_r/M_s ratio, explains the dependence of the response on the applied magnetic field. As can be observed in Table S3, Fe_3O_4, Fe_3O_4-Cu, Fe_3O_4-Ag, and Fe_3O_4-Au exhibit an extremely low magnetic squareness (SQ): 0.04 for Fe_3O_4-Au and 0.05 for Fe_3O_4-Ag. A remarkably high SQ (0.24) was obtained for bare magnetite Fe_3O_4 since a magnetic moment with a strong dependence on the applied field is desired ($M_r/M_s \rightarrow 0$). These results show that the addition of metallic clusters such as Cu, Ag, and Au is beneficial from the catalytic and magnetic points of view.[47]

Catalytic Activity. Since it is difficult to obtain the reduction potential for the nitro group , ascorbic acid and $NaBH_4$ were used as control (yield < 10%) to discard any spontaneous reaction (Figure 5). Fe_3O_4-Cu, Fe_3O_4-Ag, and Fe_3O_4-Au were used for the reduction of NA, giving the yield of 70−80%, showing that if G11 metals are presented, the yield has been increased to 82.56% for Fe_3O_4-Cu's conversion of NA to oligomers, which would be further increased to 87.8 and 91.3%, respectively, if ascorbic acid or $NaBH_4$ were added. The oligomer conversion was 93.4 and 96.6% for Fe_3O_4-Ag and Fe_3O_4-Au, respectively, without any additional reducing agents. From the conversion point of view, all catalysts show a similar behavior for a reduction reaction longer than 60 min. However, the kinetic results demonstrate that the presence of Ag and, especially, Au accelerates the reaction rate. For Fe_3O_4-Cu, the conversion was 82.5% after 30 min and for Fe_3O_4-Au, it was >90% even at less than 10 min, showing that Au influences significantly the crystalline and catalytic performances. The reduction reaction follows a first-order

kinetics, showing that Fe_3O_4-Au is the best catalyst with a reaction rate ($k_{Fe_3O_4-Au}$ = 0.416 mM L^{-1} min^{-1}) of 20 times greater than that of bare Fe_3O_4 ($k_{Fe_3O_4}$ = 0.018 mM L^{-1} min^{-1}). The reduction rate increased when we added $NaBH_4$ (k = 1.04 mM L^{-1} min^{-1}) to the medium ($t_{1/2}$ < 1.6 min). In contrast, the reduction rate for Fe_3O_4-Cu ($k_{Fe_3O_4-Cu}$ = 1.04 mM L^{-1} min^{-1}) or Fe_3O_4-Ag is slower even in the presence of $NaBH_4$, with half-lives significantly greater for Cu ($t_{1/2}$ = 3.39 min) and Ag ($t_{1/2}$ = 2.88 min) (Figure S4).

Magnetite is a stable material and it has 2/3 of Fe^{3+} in Fe_3O_4, making it an electron-rich center for the interaction with aromatic amines to form azo bonds, liberating H^+, while 1/3 of the Fe^{2+} in magnetite is less stable. After the Fe^{3+} active sites are engaged with NA and iron(II) is involved in the reaction in the presence of water.[48]

Among the samples, for Fe_3O_4-Ag, Ag^0 slowly transforms into Ag^+, which improves its efficiency. For the Fe_3O_4-Au sample, on the other hand, gold is resistant, behaving as a strong oxidizing agent. Moreover, the SPR of noble metals (Ag and Au) can increase the electron mobility, acting as electron sinks at the material interface centers that reduce the electron density (δ^-) in alcohol (in the solvent system), enhancing further the reduction potential.[49] It has also been theorized that at the surface of the catalysts, the Fe_3O_4 matrix can react with H^+ and H_3O^+ to form Fe_3O_3-Au-H type intermediates.[50] The recyclability studies of catalysts were not attempted; however, these materials have been steadily prepared in the laboratory and in our previous works, our group demonstrated the feasibility of the sample recuperation due to their magnetic properties.[51]

Product Analysis. The NA reduction was studied by ^{1}H NMR (Figure S5a). In the aromatic region (Figure S6b), three signals are presented corresponding to aromatic amines ($\delta \approx$ 6.5 ppm) at the beginning of the reduction (T_0) and deshielded hydrogens within the aromatic center ($\delta \approx$ 8.2 ppm). The formation of imine/azo groups typically detected at $\delta \approx$ 10.1 ppm shows that NA exists in equilibrium state with an azo adduct. The H_2 production from the catalyst reduces the nitro group as the signal at $\delta \approx$ 6.5 ppm quickly fades, and after 60 min (T_1), the imine signal (N=N−) is steadily presented. After T_S = 300 min, only the presence of aromatic hydrogens and imines ($\delta \approx$ 8.2 ppm) is observed, suggesting the
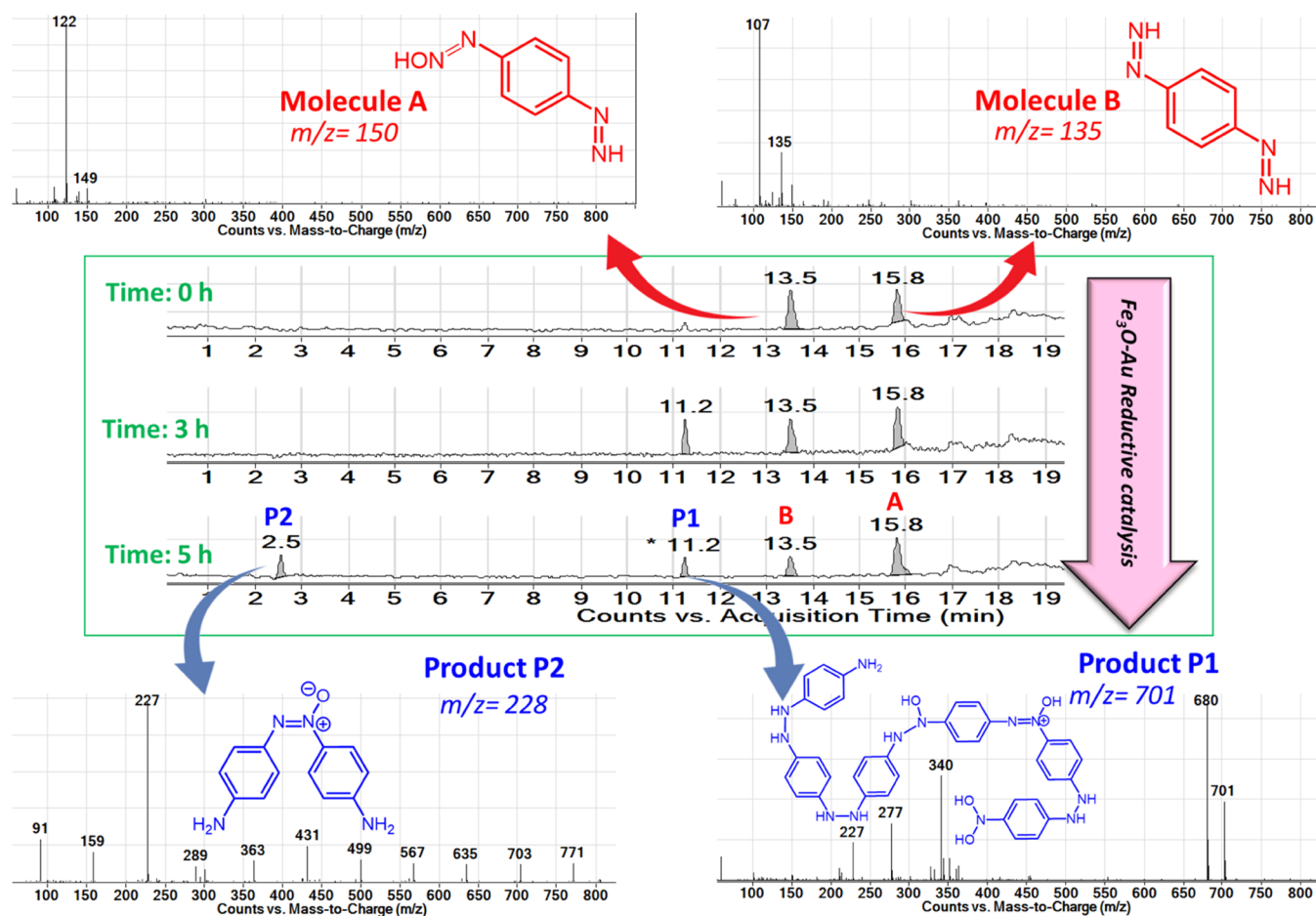
Figure 6. High-performance liquid chromatography-mass spectrometry (HPLC-MS) studies for product analysis in reduction of NA by Fe_3O_4-Au.

reduction of NA, which is consistent with the reported studies.[52]

The product formation was also analyzed by liquid chromatography (Figure 6). At time = 0 min, in the reduction reaction, NA shows small amounts of a mixture of two semicompounds (molecule A, T_R = 13.6 min, $C_6H_4N_3O_2^+$, m/z = 150, and molecule B, T_R = 15.89 min, $C_6H_6N_4$, m/z = 135). These two molecules are part of a residual emerging from the natural decay of NA.[53] After 3.0 h of the reaction, a new peak corresponding to product P1 at T_R = 11.2 min ($C_{36}H_{37}N_{12}O_4^+$, m/z = 701) is detected, and after 5.0 h, along with the signal of P1, another peak corresponding to product P2 at T_R = 2.6 min ($C_{12}H_{12}N_4O$, m/z = 228) is observed. Both of these products are formed from the reduction of R-NO_2 groups through imine linkage. For P1, the oligomer structure consists of six aromatic groups, while for P2, it contains two rings. The additional signals evidently correspond to aniline, m/z = 94.

After analyzing the above results, a mechanism is proposed whereby NA undergoes polymeric catalytic reactions in which molecules A and B are formed as cationic fragments, as observed by LC-MS (Scheme 1). In the catalytic reaction, the catalytic material gives away two electrons, which interact with water to produce H_2 and OH^- ions. In the first step, with two electrons, the $-NO_2$ group converts to $-N{=}O$ (I), which undergoes a reduction to the $-NH\text{-}OH$ group (II). In the second step, $-N{=}O$ and $-NH\text{-}OH$ undergo a reaction to form the diazo link $-N{=}N-$ (III), which can be reduced to $-NH-NH-$ (IV). Furthermore, another molecule of $-N{=}O$

(I) reacts with molecule III to form molecule IV, which undergoes a reduction to give molecule V through catalytic reduction. This reaction is repeated three times after taking three molecules of I with molecule V to form VI. The reduction of nitroaniline is normally related to the Haber reaction: the condensation of nitrosoaniline with another nitroaniline to form azoxyaniline structures. If this process further proceeds, a secondary process takes place, involving the formation of hydrazoaniline, yielding imines and H_2O, O_2, and H^+.[54] For Fe_3O_4-Au, NPs enhance amine reduction and facilitate azo polymerization by dendrimeric growth.[55] Under the studied conditions (20 °C, 101.3 kPa), a maximum number of 6 bound units is detected and there could be a greater degree of oligomerization if the temperature and pressure are increased.

Carbon Balance Analysis. The total carbon balance of oligomerization of nitroaniline was analyzed (Figure 7), observing that the total amount of carbon in the system remains stable without any further carbon fixation from the environment.[56] For example, the TOC is 84.67 mg/L at the initial time, coinciding approximately to the theoretical value of 72 mg/L for NA (1.0 mM). However, this value is increased modestly to 95.20, 97.27, and 96.34 mg/L for Fe_3O_4-Au, Fe_3O_4-Ag, and Fe_3O_4-Cu, respectively (calculated error, σ = 8.65). The slight increase of organic carbon is probably attributed to the reduction of trace amounts of carbonate salts in water.[57] The concentration of COD in the oligomerization shows a considerable change; for instance, initially, the COD

Scheme 1. Proposed Mechanism for the Reduction of 4-Nitroaniline by Fe$_3$O$_4$-M (Au, Ag, Cu)
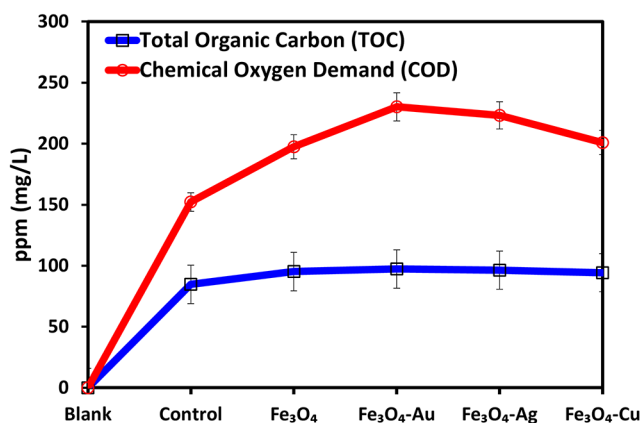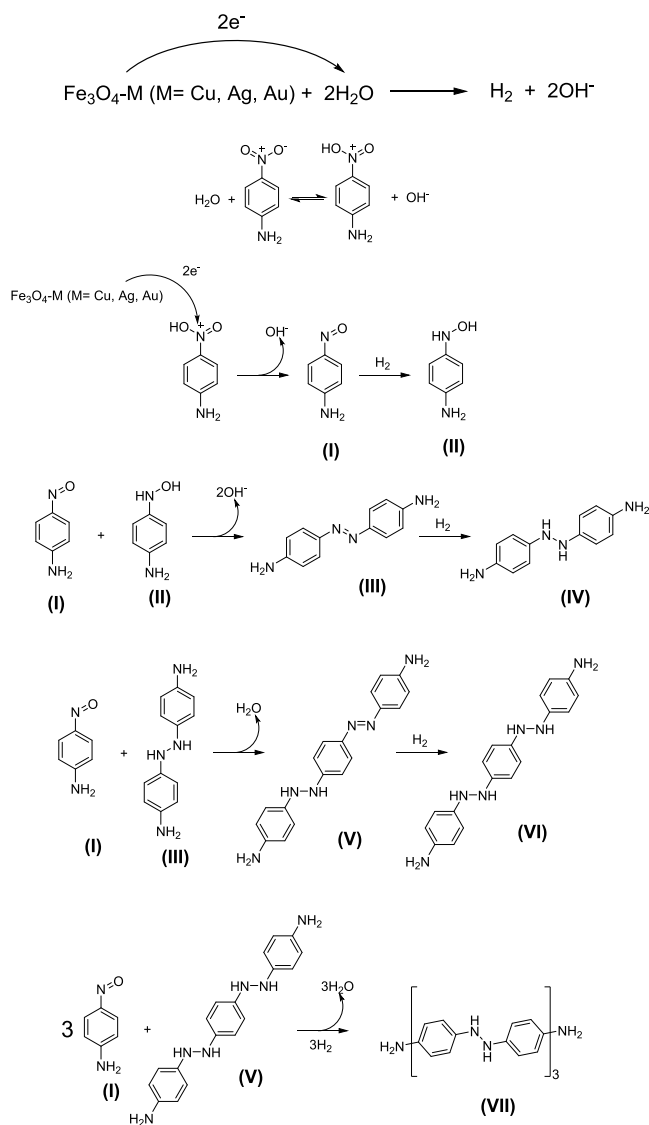

Figure 7. Carbon−oxygen balance for oligomerization of 4-nitroaniline by Fe$_3$O$_4$-based catalysts.

means that azo linkages involve in the reduction process, requiring an oxidizing agent such as O$_2$, which is inversely proportional to the number of oligomers formed upon the catalyzed reduction. Thus, for bare Fe$_3$O$_4$, the COD was 197 mg/L, while for Fe$_3$O$_4$-Au, Fe$_3$O$_4$-Ag, and Fe$_3$O$_4$-Cu, the value was increased to 230, 223.26, and 200.93 mg/L, respectively (standard deviation or error σ = 8.84).
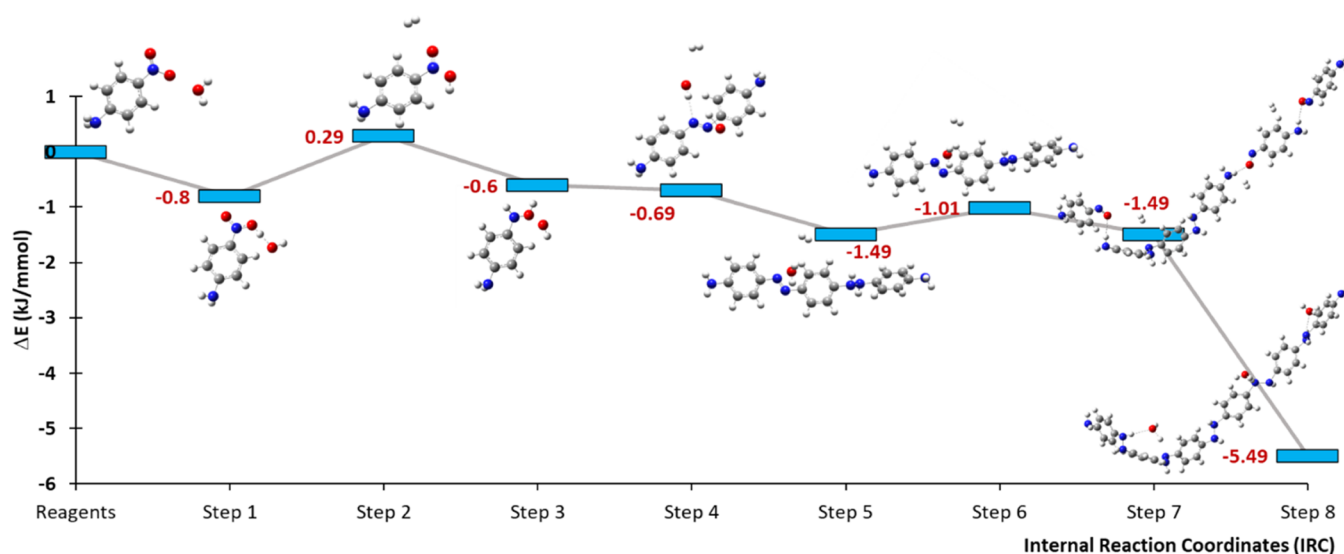
Mechanism Modeling. The reduction of 4-NA was computationally studied using density functional theory (DFT) calculations, and the geometries at the stationary point were optimized at each reaction step with B3LYP[58] at 6-311G(d,p).[58b] The reduction of NA by Fe$_3$O$_4$ yields the formation of two products; the total energy for the feasibility formation was analyzed thermodynamically (Figure S6).

In the proposed pathway (Scheme 1), several steps were involved in the reduction of NA and they were modeled by DFT (Figure S7). The total energy of each system allowed us to find out the minimum energy of the system that supports the oligomerization of nitroaniline under the catalytic reduction by Fe$_3$O$_4$-Au. The geometrical optimization associated with a minimum energy of the nitroaniline reduction products was calculated in an aqueous environment (Figures 8 and S8). In step 1, −NO$_2$ undergoes a reduction by the catalytic material as this is favored at −0.8 kJ/mmol. Step 2 involves further reduction of the nitro group to form an oxime although we were unable to detect this in the chromatographic analysis as its formation required a greater energy (ΔE = 0.29 kJ/mmol), which would be associated with the rate-determining step. In step 3 and step 4, the low energy couplings are favored because of the reaction of a nitroso group with amine to release of 0.69 kJ/mmol for the dimer formation, while the energy release of 1.01 kJ/mmol is for the trimerization. The metallic clusters promote e- mobility, which generates additional adducts to trigger finally the oligomeric production in step 5. The final product consists of 6 aromatic rings formed by an exothermic reaction (ΔE_t = −5.09 kJ/mmol) and the formation of the immediate precursor with ΔE = −4.0 kJ/mmol (step 7). This additional release of energy could further contribute to a self-maintaining reaction, and it enhances further the reduction potential of the system. This observation suggests that a metallic surface allows the reduction reaction. This explains the identification of simple dimers P1 after several hours of reaction ($t > 3$ h) and the product P2 can be easily formed, but it was not seen in the reduction reaction. So, in the presence of Fe$_3$O$_4$-M (M = Cu, Ag, Au), NA undergoes oligomerization.

■ EXPERIMENTAL SECTION

Materials and Methods. All reagents and solvents used in the studies were as received from the chemical company without any further purification: HAuCl$_4$, FeCl$_3$·6H$_2$O, CH$_3$COONa, Ni(NO$_3$)$_2$, Cu(NO$_3$)$_2$, NaBH$_4$, AgNO$_3$, and Na$_2$CO$_3$ (Merck-Aldrich).

Characterization. XRD analyses were conducted using a D8 Advance Davini diffractometer with Ni-filtered Cu Kα radiation (λ = 1.541Å) with a Theta-Theta Bruker AXS configuration (diffraction angle at 2θ: 20−80° operating at a voltage of 40 kV, 30 mA). Scanning electron microscopy was performed using a JEOL JSM-5900 at 20 kV. Energy dispersive X-ray spectroscopy analyses were also performed using an Oxford ISIS EDS analyzer coupled to the SEM, for which 15 sample spots were taken, the elemental composition was measured, and the average results were used to determine the

concentration (control) is 157.1 ± 8.38 mg/L and it has been increased if oligomerization occurs from the reduction of NA in the presence of Fe$_3$O$_4$-Cu, Fe$_3$O$_4$-Ag, or Fe$_3$O$_4$-Au. This

Figure 8. DFT total energy determined for the products (oligomerization) formed in the 4-NA reduction in the presence of Fe_3O_4-Au (pathway 1 in blue; pathway 2 in red).

Scheme 2. Preparation of Fe_3O_4 Doping of Group 11 Metals
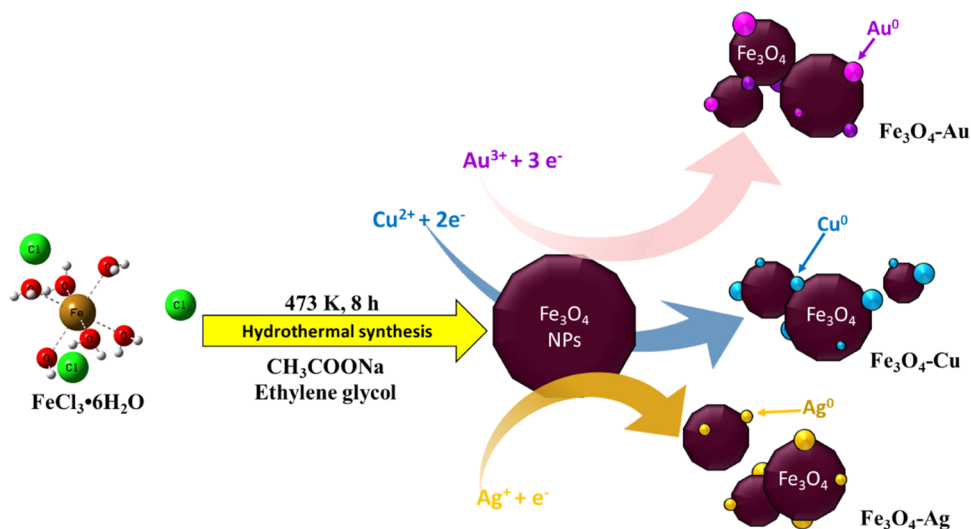
elemental composition of the sample.[59] Transmission electron microscopy was carried out using a JEOL-JEM 2010 microscope equipped with a LaB_6 thermo-ionic cannon and the crystalline nature was studied.[60] XPS studies were performed using a K-Alpha Thermo-Fisher; the images were collected with a pass energy of 80 eV, and the oxidation state of metal ions was analyzed. Magnetic studies were done using a Quantum Design MPMS3 Squid AC magnetometer at 300 K and in the range of −50 kOe < H < 50 kOe (H ± 5.0 T). Absorbance measurements were performed using a Perkin Elmer Lambda 25 UV-Vis spectrophotometer. In the reduction of 4-NP, the product analysis was studied by ^1H NMR using a 400 MHz Varian VNRMS; the separation of products was done by an Agilent 1200 HPLC equipped with a 300 mm C-18 column and the effluent was injected into an Agilent 6410 triple quadrupole for ESI+ analysis.

Synthesis of Nanocatalysts. Magnetite nanoparticles were prepared as reported previously.[61] $FeCl_3 \cdot 6H_2O$ was mixed with CH_3COONa in ethylene glycol, and the resulting mixture was stirred and transferred to a stainless-steel

autoclave for heating for 8 h at 473 K. The product isolated was washed three times with ethanol to yield a fine black powder Fe_3O_4, to which Cu NPs or Ag NPs or Au NPs were doped by the reduction of $Cu(NO_3)_2$ or $AgNO_3$ or $HAuCl_4$ to obtain Fe_3O_4-Cu NPs or Fe_3O_4-Ag NPs or Fe_3O_4-Au NPs, respectively (Scheme 2).

Catalytic Reduction of Nitrobenzene. To analyze the photocatalytic activity of magnetite nanoparticles, the reduction kinetics of 4-nitroaniline (NA) was determined as follows: A certain amount of NA (0.01 mmol) was added to a flask containing 10.0 mL of a 5:95 of 2-propanol/H_2O solution as a solvent system. In this mixture, the prepared catalysts were dispersed in the solution with a concentration of 50.0 ppm. This mixture is allowed to react at room conditions (STR) under stirring in the absence of light. The solution was taken at different time intervals to measure the NA concentration by recording UV-Vis spectra from 200 to 900 nm and the intensity of the peak corresponding to 4-nitroaniline (λ_{max}, 380 nm) was determined. In product analysis using ^1H NMR, a sample of Fe_3O_4-Au (50 ppm) was left to react with NA (0.1

mM) for 5 h, and the substrate and 2-propanol (0.01 mM) were used in the ratio 5:95 in D_2O. In the case of HPLC-MS studies, the same procedure was followed with a subsequent injection using a mobile phase consisting of water and CN (90:10) with 0.1% of formic acid.

Carbon Balance Analysis. The carbon balance and oxygen demands were determined after the formation of oligomerization from 4-nitroaniline. Total Organic Carbon (TOC) and Chemical Oxygen demand (COD) were estimated on a GE Sievers Innovox instrument using $KMnO_4$ as an oxidizing agent.

Theoretical Studies. *DFT Modeling.* Energy determination was carried out using an unrestricted HSEh1PBE/LANL2DZ basis set for a full-set population analysis. The calculated model consists of 4 cubic spinel Fe_3O_4 cells attached to an Au_8 gold bipyramidal (D5h) cluster.

Structural Optimization of Oligomers. The reduction of 4-NA was computationally studied using the DFT calculations,[55−57] and the geometries at stationary point at each reaction step were studied with B3LYP[58] at 6-311G(d,p).[58b] The unrestricted B3LYP calculations were used wherever radical systems were involved, and for relative reactivity trend, the UB3LYP/6-311G(d,p) was employed because of its high reliability.[62] In a PCM model, the solvent medium (water as a solvent) was considered. The total energy and vibrational frequencies were determined in each step of the mechanism using the optimized geometries as inputs, and the corresponding transition states (TS) were determined by a QST3 calculation using the BB1K set developed by Becke.[63] The DFT modeling consisted of a system containing 126 atoms (C = 36, H = 52, O = 22, N = 16) and 556 electrons. The starting geometry ($C_{36}H_{52}N_{16}O_{22}$) consisted of four 1,4-nitroaniline and two 1,4-bis(dianzenyl)benzene molecules complemented with 14 ^-OH groups in an aqueous solvent system. For every step in the mechanism, the total system energy was determined, and individual molecular local optimizations were conducted. For the computational work, a B3LYP functional coupled to a 6-311G basis set was used in a polarizable continuum model of water.

CONCLUSIONS

In the present work, the oligomerization of p-nitroaniline was achieved via azo bonding using Fe_3O_4-Cu NPs, Fe_3O_4-Ag NPs, or Fe_3O_4-Au NPs. The reduction reaction follows a pseudo-first-order kinetics, and for Fe_3O_4-Au, the reaction rate is $k = 1.04$ mM L^{-1} min^{-1} (97%). HPLC-MS showed the formation of a six-unit oligomer ($C_{36}H_{37}N_{12}O_4$) and a dimer ($C_{12}H_{12}N_4O$) as the main products, for which a mechanism of NA reduction is proposed. To prove further the feasibility of the reaction, a DFT model was applied to a system consisting of 36 C, 52 H, 16 N, and 22 O in a PCM model. The present study describes the development of nanocatalysts for the reduction of NA to avoid its environmental implications.

ASSOCIATED CONTENT

ⓢ Supporting Information

The Supporting Information is available free of charge at https://pubs.acs.org/doi/10.1021/acsomega.2c06326.

> Preparation details of nanoparticles, powder X-ray diffraction (PXRD), EDS elemental analysis, X-ray photoelectron spectroscopy (XPS), magnetic parameters, minetics of nitroaniline reduction, ^1H NMR kinetics

for reduction of nitroaniline by Fe_3O_4-Au; proposed mechanism for formation of P1 by oligomeric reduction of p-nitroaniline by Fe_3O_4-Au; electrostatic potential mapping of key states during NA reduction (PDF)

AUTHOR INFORMATION

Corresponding Authors

Carlos Alberto Huerta-Aguilar − *School of Engineering and Sciences, Tecnologico de Monterrey, 72453 Puebla, Mexico;* ⓞ orcid.org/0000-0001-9274-5330; Email: huertaa@tec.mx

Pandiyan Thangarasu − *Faculty of Chemistry, National Autonomous University of Mexico (UNAM), 04510 Mexico City, Mexico;* ⓞ orcid.org/0000-0001-7302-4044; Email: pandiyan@unam.mx

Authors

Rajendra Srivastava − *Department of Chemistry, Indian Institute of Technology Ropar, Rupnagar 140001 Panjab, India;* ⓞ orcid.org/0000-0003-2271-5376

Jesús A. Arenas-Alatorre − *Instituto de Física, Universidad Nacional Autónoma de México (UNAM), 04510 México, D. F., México*

Complete contact information is available at:
https://pubs.acs.org/10.1021/acsomega.2c06326

Notes

The authors declare no competing financial interest.
The authors declare no competing financial interest. The data that support the findings of this study are available in the supplementary material of this article.

REFERENCES

(1) Wei, W.; Sun, R.; Jin, Z.; Cui, J.; Wei, Z. G. Hydroxyapatite-gelatin nanocomposite as a novel adsorbent for nitrobenzene removal from aqueous solution. *Appl. Surf. Sci.* **2014**, *292*, 1020−1029.

(2) (a) Sheng, T.; Qi, Y. J.; Lin, X.; Hu, P.; Sun, S. G.; Lin, W. F. Insights into the mechanism of nitrobenzene reduction to aniline over Pt catalyst and the significance of the adsorption of phenyl group on kinetics. *Chem. Eng. J.* **2016**, *293*, 337−344. (b) Cyr, A.; Huot, P.; Marcoux, J. F.; Belot, G.; Laviron, E.; Lessard, J. The electrochemical reduction of nitrobenzene and azoxybenzene in neutral and basic aqueous methanolic solutions at polycrystalline copper and nickel electrodes. *Electrochim. Acta* **1989**, *34*, 439−445.

(3) Turáková, M.; Salmi, T.; Eranen, K.; Warna, J.; Murzin, D. Y.; Kralik, M. Liquid phase hydrogenation of nitrobenzene. *Appl. Catal., A* **2015**, *499*, 66−76.

(4) (a) Silva, M. A. R.; Testolin, R. C.; Godinho-Castro, A. P.; Correa, A. X. R.; Radetski, C. M. Environmental impact of industrial sludge stabilization/solidification products: Chemical or ecotoxicological hazard evaluation? *J. Hazard. Mater.* **2011**, *192*, 1108−1113. (b) Qian, G. Q.; Duanmu, C.; Ali, N.; Khan, A.; Malik, S.; Yang, Y.; Bilal, M. Hazardous wastes, adverse impacts, and management strategies: a way forward to environmental sustainability. *Environ. Dev. Sustainability* **2022**, *24*, 9731−9756.

(5) Kadam, H. K.; Tilve, S. G. Advancement in methodologies for reduction of nitroarenes. *RSC Adv.* **2015**, *5*, 83391−83407.

(6) (a) Fan, G. Y.; Wang, Y. H.; Wang, C. Y. One-pot synthesis of aluminum oxyhydroxide matrix-entrapped Pt nanoparticles as an excellent catalyst for the hydrogenation of nitrobenzene. *RSC Adv.* **2014**, *4*, 10997−11002. (b) Easterday, R.; Sanchez-Felix, O.; Losovyj, Y.; Pink, M.; Stein, B. D.; Morgan, D. G.; Rakitin, M.; Doluda, V. Y.; Sulman, M. G.; Mahmoud, W. E.; Al-Ghamdi, A. A.; Bronstein, L. M. Design of ruthenium/iron oxide nanoparticle mixtures for hydrogenation of nitrobenzene. *Catal. Sci. Technol.* **2015**, *5*, 1902−1910.

(7) (a) Torres, C.; Campos, C.; Fierro, J. L. G.; Oportus, M.; Reyes, P. Nitrobenzene Hydrogenation on Au/TiO₂ and Au/SiO₂ Catalyst: Synthesis, Characterization and Catalytic Activity. *Catal. Lett.* **2013**, *143*, 763−771. (b) Roy, P.; Periasamy, A. P.; Liang, C. T.; Chang, H. T. Synthesis of Graphene-ZnO-Au Nanocomposites for Efficient Photocatalytic Reduction of Nitrobenzene. *Environ. Sci. Technol.* **2013**, *47*, 6688−6695. (c) Kartusch, C.; Makosch, M.; Sa, J.; Hungerbuehler, K.; van Bokhoven, J. A. The Dynamic Structure of Gold Supported on Ceria in the Liquid Phase Hydrogenation of Nitrobenzene. *ChemCatChem* **2012**, *4*, 236−242.

(8) (a) Hashmi, A. S. K. Introduction: Gold Chemistry. *Chem. Rev.* **2021**, *121*, 8309−8310. (b) Hashmi, A. S. K.; Hutchings, G. J. Gold catalysis. *Angew. Chem., Int. Ed.* **2006**, *45*, 7896−7936.

(9) Subramanian, T.; Pitchumani, K. Selective Reduction of Nitroarenes by using Zeolite-Supported Copper Nanoparticles with 2-Propanol as a Sustainable Reducing Agent. *ChemCatChem* **2012**, *4*, 1917−1921.

(10) El Maksod, I. H. A.; Hegazy, E. Z.; Kenawy, S. H.; Saleh, T. S. An Environmentally Benign, Highly Efficient Catalytic Reduction of p-Nitrophenol using a Nano-Sized Nickel Catalyst Supported on Silica-Alumina. *Adv. Synth. Catal.* **2010**, *352*, 1169−1178.

(11) (a) Cárdenas-Lizana, F.; Keane, M. A. The development of gold catalysts for use in hydrogenation reactions. *J. Mater. Sci.* **2013**, *48*, 543−564. (b) Antonetti, C.; Oubenali, M.; Galletti, A. M. R.; Serp, P.; Vannucci, G. Novel microwave synthesis of ruthenium nanoparticles supported on carbon nanotubes active in the selective hydrogenation of p-chloronitrobenzene to p-chloroaniline. *Appl. Catal. A-Gen.* **2012**, *421*−*422*, 99−107.

(12) Yarzhemsky, V. G.; Murav'ev, E. N.; Kazaryan, M. A.; Dyakov, Y. A. Electronic structure of gold nanoparticles. *Inorg. Mater.* **2012**, *48*, 1075−1077.

(13) (a) Jagadeesh, R. V.; Surkus, A. E.; Junge, H.; Pohl, M. M.; Radnik, J.; Rabeah, J.; Huan, H. M.; Schunemann, V.; Bruckner, A.; Beller, M. Nanoscale Fe₂O₃-Based Catalysts for Selective Hydrogenation of Nitroarenes to Anilines. *Science* **2013**, *342*, 1073−1076. (b) Westerhaus, F. A.; Jagadeesh, R. V.; Wienhofer, G.; Pohl, M. M.; Radnik, J.; Surkus, A. E.; Rabeah, J.; Junge, K.; Junge, H.; Nielsen, M.; Bruckner, A.; Beller, M. Heterogenized cobalt oxide catalysts for nitroarene reduction by pyrolysis of molecularly defined complexes. *Nature Chem.* **2013**, *5*, 537−543.

(14) Cai, S. F.; Duan, H. H.; Rong, H. P.; Wang, D. S.; Li, L. S.; He, W.; Li, Y. D. Highly Active and Selective Catalysis of Bimetallic Rh3Ni1 Nanoparticles in the Hydrogenation of Nitroarenes. *ACS Catal.* **2013**, *3*, 608−612.

(15) (a) Lyu, J. H.; Wang, J. G.; Lu, C. S.; Ma, L.; Zhang, Q. F.; He, X. B.; Li, X. N. Size-Dependent Halogenated Nitrobenzene Hydrogenation Selectivity of Pd Nanoparticles. *J. Phys. Chem. C* **2014**, *118*, 2594−2601. (b) Turáková, M.; Kralik, M.; Lehocky, P.; Pikna, L.; Smrtova, M.; Remeteiova, D.; Hudak, A. Influence of preparation method and palladium content on Pd/C catalysts activity in the liquid phase hydrogenation of nitrobenzene to aniline. *Appl. Catal., A* **2014**, *476*, 103−112.

(16) (a) Malaika, A.; Kozlowski, M. Modification of activated carbon with different agents and catalytic performance of products obtained in the process of ethylbenzene dehydrogenation coupled with nitrobenzene hydrogenation. *Chem. Eng. J.* **2011**, *171*, 1348−1355. (b) Xie, M.; Zhang, F. W.; Long, Y.; Ma, J. T. Pt nanoparticles supported on carbon coated magnetic microparticles: an efficient

recyclable catalyst for hydrogenation of aromatic nitro-compounds. *RSC Adv.* **2013**, *3*, 10329−10334.

(17) (a) Zhang, F. W.; Jin, J.; Zhong, X.; Li, S. W.; Niu, J. R.; Li, R.; Ma, J. T. Pd immobilized on amine-functionalized magnetite nanoparticles: a novel and highly active catalyst for hydrogenation and Heck reactions. *Green Chem.* **2011**, *13*, 1238−1243. (b) Gupta, A. K.; Gupta, M. Synthesis and surface engineering of iron oxide nanoparticles for biomedical applications. *Biomaterials* **2005**, *26*, 3995−4021.

(18) (a) Choi, S.-H.; Na, H. B.; Park, Y. I.; An, K.; Kwon, S. G.; Jang, Y.; Park, M.-h.; Moon, J.; Son, J. S.; Song, I. C.; Moon, W. K.; Hyeon, T. Simple and Generalized Synthesis of Oxide−Metal Heterostructured Nanoparticles and their Applications in Multimodal Biomedical Probes. *J. Am. Chem. Soc.* **2008**, *130*, 15573−15580. (b) Qu, X.; Alvarez, P. J. J.; Li, Q. Applications of nanotechnology in water and wastewater treatment. *Water Res.* **2013**, *47*, 3931−3946. (c) Xu, P.; Zeng, G. M.; Huang, D. L.; Feng, C. L.; Hu, S.; Zhao, M. H.; Lai, C.; Wei, Z.; Huang, C.; Xie, G. X.; Liu, Z. F. Use of iron oxide nanomaterials in wastewater treatment: A review. *Sci. Total Environ.* **2012**, *424*, 1−10. (d) Chauhan, N.; Narang, J.; Jain, U. Amperometric acetylcholinesterase biosensor for pesticides monitoring utilising iron oxide nanoparticles and poly(indole-5-carboxylic acid). *J. Exp. Nanosci.* **2016**, *11*, 111−122.

(19) (a) Latiff, N. M.; Mayorga-Martinez, C. C.; Khezri, B.; Szokolova, K.; Sofer, Z.; Fisher, A. C.; Pumera, M. Cytotoxicity of layered metal phosphorus chalcogenides (MPXY) nanoflakes; FePS3, CoPS3, NiPS3. *FlatChem* **2018**, *12*, 1−9. (b) Wang, D.; Yin, F.; Du, Z.; Han, D.; Tang, J. Recent progress in quantum dot-sensitized solar cells employing metal chalcogenides. *J. Mater. Chem. A* **2019**, *7*, 26205−26226.

(20) Gawande, M. B.; Rathi, A. K.; Branco, P. S.; Nogueira, I. D.; Velhinho, A.; Shrikhande, J. J.; Indulkar, U. U.; Jayaram, R. V.; Ghumman, C. A. A.; Bundaleski, N.; Teodoro, O. Regio- and Chemoselective Reduction of Nitroarenes and Carbonyl Compounds over Recyclable Magnetic Ferrite-Nickel Nanoparticles (Fe3O4-Ni) by Using Glycerol as a Hydrogen Source. *Chem. - Eur. J.* **2012**, *18*, 12628−12632.

(21) (a) Wang, F.; Liu, J.; Xu, X. Layered material gamma-ZrP supported platinum catalyst for liquid-phase reaction: a highly active and selective catalyst for hydrogenation of the nitro group in para-chloronitrobenzene. *Chem. Commun.* **2008**, 2040−2042. (b) Liu, L. Q.; Qiao, B. T.; Chen, Z. J.; Zhang, J.; Deng, Y. Q. Novel chemoselective hydrogenation of aromatic nitro compounds over ferric hydroxide supported nanocluster gold in the presence of CO and H2O. *Chem. Commun.* **2009**, 653−655.

(22) (a) Lee, J.; Kwon, S. G.; Park, J.-G.; Hyeon, T. Size Dependence of Metal−Insulator Transition in Stoichiometric Fe₃O₄ Nanocrystals. *Nano Lett.* **2015**, *15*, 4337−4342. (b) Smirnov, A. V.; Tarduno, J. A. Magnetic field control of the low-temperature magnetic properties of stoichiometric and cation-deficient magnetite. *Earth Planetary Sci. Lett.* **2002**, *194*, 359−368.

(23) (a) Vieira, Y.; Silvestri, S.; Leichtweis, J.; Jahn, S. L.; de Moraes Flores, E. M.; Dotto, G. L.; Foletto, E. L. New insights into the mechanism of heterogeneous activation of nano−magnetite by microwave irradiation for use as Fenton catalyst. *J. Environ. Chem. Eng.* **2020**, *8*, No. 103787. (b) Periyasamy, M.; Sain, S.; Ghosh, E.; Jenkinson, K. J.; Wheatley, A. E. H.; Mukhopadhyay, S.; Kar, A. Visible light photocatalysts from low-grade iron ore: the environmentally benign production of magnetite/carbon (Fe₃O₄/C) nano-composites. *Environ. Sci. Pollut. Res.* **2022**, *29*, 6698−6709.

(24) (a) Mishra, A.; Mishra, A.; Pandey, A. Study of organic pollutant removal capacity and work function of magnetite/graphene oxide nanocomposites. *Mater. Res. Express* **2019**, *6*, No. 125039. (b) Kulpa-Koterwa, A.; Ossowski, T.; Niedzialkowski, P. Functionalized Fe₃O₄ Nanoparticles as Glassy Carbon Electrode Modifiers for Heavy Metal Ions Detection-A Mini Review. *Materials* **2021**, *14*, No. 7725. (c) Siregar, J.; Septiani, N. L. W.; Abrori, S. A.; Sebayang, K.; Irzaman; Fahmi, M. Z.; Humaidi, S.; Sembiring, T.; Sembiring, K.; Yuliarto, B. Review-A Pollutant Gas Sensor Based On Fe₃O₄

Nanostructures: A Review. *J. Electrochem. Soc.* **2021**, *168*, No. 027510. (d) Qin, M.; Xu, M. J.; Niu, L. L.; Cheng, Y. Z.; Niu, X. L.; Kong, J. L.; Zhang, X. M.; Wei, Y.; Huang, D. Multifunctional modification of Fe3O4 nanoparticles for diagnosis and treatment of diseases: A review. *Front. Mater. Sci.* **2021**, *15*, 36–53. (e) Dong, L. N.; Chen, G.; Liu, G. Y.; Huang, X. D.; Xu, X. M.; Li, L. Y.; Zhang, Y. G.; Wang, J.; Jin, M. J.; Xu, D. H.; Abd El-Aty, A. M. A review on recent advances in the applications of composite Fe₃O₄ magnetic nanoparticles in the food industry. *Crit. Rev. Food Sci. Nutr.* **2022**, 1–29.

(25) (a) Das, A.; Han, Z. J.; Haghighi, M. G.; Eisenberg, R. Photogeneration of hydrogen from water using CdSe nanocrystals demonstrating the importance of surface exchange. *Proc. Nat. Acad. Sci. U.S.A.* **2013**, *110*, 16716–16723. (b) Yu, W. W.; Qu, L. H.; Guo, W. Z.; Peng, X. G. Experimental determination of the extinction coefficient of CdTe, CdSe, and CdS nanocrystals. *Chem. Mater.* **2003**, *15*, 2854–2860. (c) Jensen, S. C.; Homan, S. B.; Weiss, E. A. Photocatalytic Conversion of Nitrobenzene to Aniline through Sequential Proton-Coupled One-Electron Transfers from a Cadmium Sulfide Quantum Dot. *J. Am. Chem. Soc.* **2016**, *138*, 1591–1600.

(26) (a) Peng, S.; Sun, S. Synthesis and Characterization of Monodisperse Hollow Fe3O4 Nanoparticles. *Angew. Chem.* **2007**, *119*, 4233–4236. (b) Jenkins, R.; Fawcett, T. G.; Smith, D. K.; Visser, J. W.; Morris, M. C.; Frevel, L. K. JCPDS — International Centre for Diffraction Data Sample Preparation Methods in X-Ray Powder Diffraction. *Powder Diffr.* **1986**, *1*, 51–63.

(27) (a) Thirupathi, B.; Smirniotis, P. G. Co-doping a metal (Cr, Fe, Co, Ni, Cu, Zn, Ce, and Zr) on Mn/TiO2 catalyst and its effect on the selective reduction of NO with NH3 at low-temperatures. *Appl. Catal., B* **2011**, *110*, 195–206. (b) Lock, N.; Jensen, E. M. L.; Mi, J.; Mamakhel, A.; Noren, K.; Meng, Q.; Iversen, B. B. Copper doped TiO₂ nanoparticles characterized by X-ray absorption spectroscopy, total scattering, and powder diffraction - a benchmark structure-property study. *Dalton Trans.* **2013**, *42*, 9555–9564.

(28) Sahai, A.; Goswami, N.; Kaushik, S. D.; Tripathi, S. Cu/Cu₂O/CuO nanoparticles: Novel synthesis by exploding wire technique and extensive characterization. *Appl. Surf. Sci.* **2016**, *390*, 974–983.

(29) Meng, Y.; Sustainable, A. Approach to Fabricating Ag Nanoparticles/PVA Hybrid Nanofiber and Its Catalytic Activity. *Nanomaterials* **2015**, *5*, 1124–1135.

(30) Mancio, A. A.; da Costa, K. M. B.; Ferreira, C. C.; Santos, M. C.; Lhamas, D. E. L.; da Mota, S. A. P.; Leão, R. A. C.; de Souza, R. O. M. A.; Araújo, M. E.; Borges, L. E. P.; Machado, N. T. Thermal catalytic cracking of crude palm oil at pilot scale: Effect of the percentage of Na₂CO₃ on the quality of biofuels. *Ind. Crops Prod.* **2016**, *91*, 32–43.

(31) Geng, G.; Chen, P.; Guan, B.; Liu, Y.; Yang, C.; Wang, N.; Liu, M. Sheetlike gold nanostructures/graphene oxide composites via a one-pot green fabrication protocol and their interesting two-stage catalytic behaviors. *RSC Adv.* **2017**, *7*, 51838–51846.

(32) Yu, J. G.; Xiang, Q. J.; Zhou, M. H. Preparation, characterization and visible-light-driven photocatalytic activity of Fe-doped titania nanorods and first-principles study for electronic structures. *Appl. Catal., B* **2009**, *90*, 595–602.

(33) Huang, Y.-F.; Zhang, L.; Ma, L.; Li, Y.; Zhong, C. Fe₃O₄@Cu/C and Fe₃O₄@CuO Composites Derived from Magnetic Metal–Organic Frameworks Fe₃O₄@HKUST-1 with Improved Peroxidase-Like Catalytic Activity. *Catal. Lett.* **2020**, *150*, 815–825.

(34) Xu, J.; Yang, H.; Fu, H.; Du, K.; Sui, Y.; Chen, J.; Zeng, Y.; Li, M.; Zou, G. Preparation and magnetic properties of magnetite nanoparticles by sol–gel method. *J. Magn. Magn. Mater.* **2007**, *309*, 307–311.

(35) Lyon, J. L.; Fleming, D. A.; Stone, M. B.; Schiffer, P.; Williams, M. E. Synthesis of Fe Oxide Core/Au Shell Nanoparticles by Iterative Hydroxylamine Seeding. *Nano Lett.* **2004**, *4*, 719–723.

(36) (a) Muhler, M.; Schlögl, R.; Ertl, G. The nature of the iron oxide-based catalyst for dehydrogenation of ethylbenzene to styrene 2. Surface chemistry of the active phase. *J. Catal.* **1992**, *138*, 413–444. (b) Yamashita, T.; Hayes, P. Analysis of XPS spectra of Fe^{2+} and Fe^{3+} ions in oxide materials. *Appl. Surf. Sci.* **2008**, *254*, 2441–2449.

(37) Chen, M.; Hu, Y.; Chen, D.; Hu, H.; Xu, Q. A novel anode for solid oxide fuel cells prepared from phase conversion of La0.3Sr0.7Fe0.7Cr0.3O3-δ perovskite under humid hydrogen. *Electrochim. Acta* **2018**, *284*, 303–313.

(38) (a) Zhu, Y.; Zhou, W.; Chen, Y.; Yu, J.; Liu, M.; Shao, Z.; High-Performance, A. Electrocatalyst for Oxygen Evolution Reaction: LiCo₀.₈Fe₀.₂O₂. *Adv. Mater.* **2015**, *27*, 7150–7155. (b) Kwan, Y. C. G.; Ng, G. M.; Huan, C. H. A. Identification of functional groups and determination of carboxyl formation temperature in graphene oxide using the XPS O 1s spectrum. *Thin Solid Films* **2015**, *590*, 40–48.

(39) Si, C.; Zhang, J.; Wang, Y.; Ma, W.; Gao, H.; Lv, L.; Zhang, Z. Nanoporous Platinum/(Mn,Al)₃O₄ Nanosheet Nanocomposites with Synergistically Enhanced Ultrahigh Oxygen Reduction Activity and Excellent Methanol Tolerance. *ACS Appl. Mater. Interfaces* **2017**, *9*, 2485–2494.

(40) Albiter, E.; Valenzuela, M. A.; Alfaro, S.; Valverde-Aguilar, G.; Martínez-Pallares, F. M. Photocatalytic deposition of Ag nanoparticles on TiO₂: Metal precursor effect on the structural and photoactivity properties. *J. Saudi Chem. Soc.* **2015**, *19*, 563–573.

(41) (a) Hsieh, P.-T.; Chen, Y.-C.; Kao, K.-S.; Wang, C.-M. Luminescence mechanism of ZnO thin film investigated by XPS measurement. *Appl. Phys. A: Mater. Sci. Process.* **2007**, *90*, 317–321. (b) Al-Gaashani, R.; Radiman, S.; Daud, A. R.; Tabet, N.; Al-Douri, Y. XPS and optical studies of different morphologies of ZnO nanostructures prepared by microwave methods. *Ceram. Int.* **2013**, *39*, 2283–2292.

(42) (a) Sureshkumar, M.; Siswanto, D. Y.; Lee, C.-K. Magnetic antimicrobial nanocomposite based on bacterial cellulose and silver nanoparticles. *J. Mater. Chem.* **2010**, *20*, 6948–6955. (b) Ateş, A.; Yanmaz, E. The effects of Ag addition and magnetic field on melt-processed YBa2Cu3Ox superconductors. *J. Alloys Compd.* **1998**, *279*, 220–228.

(43) (a) Munoz, M.; de Pedro, Z. M.; Casas, J. A.; Rodriguez, J. J. Preparation of magnetite-based catalysts and their application in heterogeneous Fenton oxidation — A review. *Appl. Catal., B* **2015**, *176–177*, 249–265. (b) Zhang, S.; Zhao, X.; Niu, H.; Shi, Y.; Cai, Y.; Jiang, G. Superparamagnetic Fe3O4 nanoparticles as catalysts for the catalytic oxidation of phenolic and aniline compounds. *J. Hazard. Mater.* **2009**, *167*, 560–566.

(44) (a) Raghu, M. S.; Yogesh Kumar, K.; Prashanth, M. K.; Prasanna, B. P.; Vinuth, R.; Pradeep Kumar, C. B. Adsorption and antimicrobial studies of chemically bonded magnetic graphene oxide-Fe3O4 nanocomposite for water purification. *J. Water Process Eng.* **2017**, *17*, 22–31. (b) Wan, Z.; Wang, J. Degradation of sulfamethazine using Fe₃O₄-Mn₃O₄/reduced graphene oxide hybrid as Fenton-like catalyst. *J. Hazard. Mater.* **2017**, *324*, 653–664.

(45) Fu, P.; Chen, G.; Xu, Y.; Cai, P.; Wang, X. H. Electrodeposition and magnetic properties of ternary Fe-Co-Ni alloy nanowire arrays with high squareness ratio. *Mater. Sci.-Pol.* **2012**, *30*, 259–263.

(46) (a) Tian, Y.; Wu, D.; Jia, X.; Yu, B.; Zhan, S. Core-shell nanostructure of α-Fe₂O₃/Fe₃O₄: synthesis and photocatalysis for methyl oranges. *J. Nanomater.* **2011**, *2011*, 1–7. (b) Hou, L.; Zhang, Q.; Jérôme, F.; Duprez, D.; Zhang, H.; Royer, S. Shape-controlled nanostructured magnetite-type materials as highly efficient Fenton catalysts. *Appl. Catal., B* **2014**, *144*, 739–749.

(47) (a) Padalia, D.; Johri, U. C.; Zaidi, M. G. H. Effect of cerium substitution on structural and magnetic properties of magnetite nanoparticles. *Mater. Chem. Phys.* **2016**, *169*, 89–95. (b) Watcharenwong, A.; Bailuang, Y.; Kajitvitchyanukul, P. Synthesis and Characterization of Monodisperse Magnetite Nanoparticles by Hydrothermal Method. *Key Eng. Mater.* **2017**, *737*, 367–372.

(48) (a) Vodyanitskii, Y. N.Biogeochemical Role of Magnetite in Urban Soils (Review of Publications). In *Eurasian Soil Science*; Springer, 2013; Vol. 46, pp 317–324. (b) Colombo, U.; Gazzarrini, F.; Lanzavecchia, G.; Sironi, G. Magnetite Oxidation: A Proposed Mechanism. *Science* **1965**, *147*, 1033.

(49) Zhao, Y.; Xing, S.; Meng, X.; Zeng, J.; Yin, S.; Li, X.; Chen, Y. Ultrathin Rh nanosheets as a highly efficient bifunctional electro-

catalyst for isopropanol-assisted overall water splitting. *Nanoscale* **2019**, *11*, 9319−9326.

(50) Yang, Y.; Jiang, K.; Guo, J.; Li, J.; Peng, X.; Hong, B.; Wang, X.; Ge, H. Facile fabrication of Au/Fe3O4 nanocomposites as excellent nanocatalyst for ultrafast recyclable reduction of 4-nitropheol. *Chem. Eng. J.* **2020**, *381*, No. 122596.

(51) (a) Huerta-Aguilar, C. A.; Ramirez-Alejandre, A. A.; Thangarasu, P.; Arenas-Alatorre, J. A.; Reyes-Dominguez, I. A.; Corea, M. D. Crystal phase induced band gap energy enhancing the photo-catalytic properties of Zn-Fe2O4/Au NPs: experimental and theoretical studies. *Catal. Sci. Technol.* **2019**, *9*, 3066−3080. (b) Huerta Aguilar, C.; Pandiyan, T.; Arenas-Alatorre, J. A.; Singh, N. Oxidation of phenols by TiO2-Fe3O4-M (M = Ag or Au) hybrid composites under visible light. *Sep. Purif. Technol.* **2015**, *149*, 265−278. (c) Cervantes-Macías, A. I.; Huerta-Aguilar, C. A.; Pandiyan, T. ZnO-Fe3O4-Au Hybrid Composites for Thioanisole Oxidation Under Visible Light: Experimental and Theoretical Studies. *J. Cluster Sci.* **2017**, *28*, 1897−1922.

(52) (a) Thomas, M.; Sheikh, M. U. D.; Ahirwar, D.; Bano, M.; Khan, F. Gold nanoparticle and graphene oxide incorporated strontium crosslinked alginate/carboxymethyl cellulose composites for o-nitroaniline reduction and Suzuki-Miyaura cross-coupling reactions. *J. Colloid Interface Sci.* **2017**, *505*, 115−129. (b) Viswanathan, P.; Ramaraj, R. Gold nanodots self-assembled polyelectrolyte film as reusable catalyst for reduction of nitroaromatics. *J. Chem. Sci.* **2018**, *130*, No. 4.

(53) Lan, R.; Irvine, J. T. S.; Tao, S. Ammonia and related chemicals as potential indirect hydrogen storage materials. *Int. J. Hydrogen Energy* **2012**, *37*, 1482−1494.

(54) (a) Lin, F.-h.; Doong, R.-a. Highly efficient reduction of 4-nitrophenol by heterostructured gold-magnetite nanocatalysts. *Appl. Catal. A: Gen.* **2014**, *486*, 32−41. (b) Lin, F.-h.; Chen, W.; Liao, Y. H.; Doong, R.; Li, Y. Effective approach for the synthesis of monodisperse magnetic nanocrystals and M-Fe3O4 (M = Ag, Au, Pt, Pd) heterostructures. *Nano Res.* **2011**, *4*, 1223−1232.

(55) (a) Kurtan, U.; Baykal, A. Fabrication and characterization of Fe3O4@APTES@PAMAM-Ag highly active and recyclable magnetic nanocatalyst: Catalytic reduction of 4-nitrophenol. *Mater. Res. Bull.* **2014**, *60*, 79−87. (b) Zarei, A.; Saedi, S.; seidi, F. Synthesis and Application of Fe3O4@SiO2@Carboxyl-Terminated PAMAM Dendrimer Nanocomposite for Heavy Metal Removal. *J. Inorg. Organomet. Polym. Mater.* **2018**, *28*, 2835−2843.

(56) (a) Dignac, M. F.; Urbain, V.; Rybacki, D.; Bruchet, A.; Snidaro, D.; Scribe, P. Chemical description of extracellular polymers: Implication on activated sludge floc structure. *Water Sci. Technol.* **1998**, *38*, 45−53. (b) Piccolo, A.; Spaccini, R.; Nebbioso, A.; Mazzei, P. Carbon Sequestration in Soil by in Situ Catalyzed Photo-Oxidative Polymerization of Soil Organic Matter. *Environ. Sci. Technol.* **2011**, *45*, 6697−6702.

(57) (a) Shadman, F.; Sams, D. A.; Punjak, W. A. Significance of the reduction of alkali carbonates in catalytic carbon gasification. *Fuel* **1987**, *66*, 1658−1663. (b) Szewczyk, M.; Magre, M.; Zubar, V.; Rueping, M. Reduction of Cyclic and Linear Organic Carbonates Using a Readily Available Magnesium Catalyst. *ACS Catal.* **2019**, *9*, 11634−11639.

(58) (a) Asamoto, M.; Iwasaki, Y.; Yamaguchi, S.; Yahiro, H. Synthesis of perovsite-type oxide catalysts, Ln(Fe, Co)O^{-3} (Ln = La, Pr, Sm, Gd, Dy, Ho, Er, and Yb), from the thermal decomposition of the corresponding cyano complexes. *Catal. Today* **2012**, *185*, 230−235. (b) Frisch, M. J.; Trucks, G. W.; Schlegel, H. B.; Scuseria, G. E.; Robb, M. A.; Cheeseman, J. R.; Montgomery, J. A., Jr.; Vreven, T.; Kudin, K. N.; Burant, J. C.; Millam, J. M.; Iyengar, S. S.; Tomasi, J.; Barone, V.; Mennucci, B.; Cossi, M.; Scalmani, G.; Rega, N.; Petersson, G. A.; Nakatsuji, H.; Hada M, M.; Ehara, K. T.; Fukuda, R.; Hasegawa, J.; Ishida, M.; Honda, T. Y.; Kitao, O.; Nakai, H.; Klene, M.; Li, X.; Knox, J. E.; Hratchian, H. P.; Cross, J. B.; Adamo, C.; Jaramillo, J.; Gomperts, R.; Stratmann, R. E.; Yazyev, O.; Austin, A. J.; Cammi, R.; Pomelli, C.; Ochterski, J. W.; Ayala, P. Y.; Morokuma, K.; Voth, G. A.; Salvador, P.; Dannenberg, J. J.; Zakrzewski, V. G.;

Dapprich, S.; Daniels, A. D.; Strain, M. C.; Farkas, O.; Malick, D. K.; Rabuck, A. D.; Raghavachari, K.; Foresman, J. B.; Ortiz, J. V.; Cui, Q.; Baboul, A. G.; Clifford, S.; Cioslowski, J.; Stefanov, B. B.; Liu, G.; Liashenko, A.; Piskorz, P.; Komaromi, I.; Martin, R. L.; Fox, D. J.; Keith, T.; Al-Laham, M. A.; Peng, C. Y.; Nanayakkara, A.; Challacombe, M.; Gill, P. M. W.; Johnson, B.; Chen, W.; Wong, M. W.; Gonzalez, C.; Pople, J. A. *Gaussian 09*; Gaussian Inc.: Wallingford, CT., 2004.

(59) Kruse, N.; Chenakin, S. XPS characterization of Au/TiO2 catalysts: Binding energy assessment and irradiation effects. *Appl. Catal., A* **2011**, *391*, 367−376.

(60) Tobaldi, D. M.; Pullar, R. C.; Gualtieri, A. F.; Seabra, M. P.; Labrincha, J. A. Sol-gel synthesis, characterisation and photocatalytic activity of pure, W-, Ag- and W/Ag co-doped TiO2 nanopowders. *Chem. Eng. J.* **2013**, *214*, 364−375.

(61) Chen, F. X.; F, W. Q.; Zhou, T. Y.; Huang, W. H. Core-Shell Nanospheres (HP-Fe2O3@TiO2) with Hierarchical Porous Structures and Photocatalytic Properties. *Acta Phys.-Chim. Sin.* **2013**, *29*, 167−175.

(62) (a) Xu, Z. F.; Lin, M. C. Computational study on the mechanism and rate constant for the C6H5+C(6)H(5)NOreaction. *J. Phys. Chem. A* **2005**, *109*, 9054−9060. (b) Choi, Y. M.; Park, J.; Lin, M. C. Experimental and computational studies of the kinetics and mechanisms for C6H5 reactions with acetone-h(6) and -d(6). *J. Phys. Chem. A* **2003**, *107*, 7755−7761. (c) Tokmakov, I. V.; Lin, M. C. Kinetics and mechanism of the OH+C6H6 reaction: A detailed analysis with first-principles calculations. *J. Phys. Chem. A* **2002**, *106*, 11309−11326. (d) Cerkovnik, J.; Erzen, E.; Koller, J.; Plesnicar, B. Evidence for HOOO radicals in the formation of alkyl hydrotrioxides (ROOOH) and hydrogen trioxide (HOOOH) in the ozonation of C-H bonds in hydrocarbons. *J. Am. Chem. Soc.* **2002**, *124*, 404−409. (e) Liu, X. H.; Guo, Y.; Xu, W. J.; Wang, Y. Q.; Gong, X. Q.; Guo, Y. L.; Guo, Y.; Lu, G. Z. Catalytic properties of Pt/Al2O3 catalysts in the aqueous-phase reforming of ethylene glycol: Effect of the alumina support. *Kinet. Catal.* **2011**, *52*, 817−822. (f) Wang, H. Y.; Yi, H. H.; Tang, X. L.; Ning, P.; Yu, L. L.; He, D.; Zhao, S. Z. Catalytic hydrolysis of cos over conial mixed oxides modified by lanthanum. *Fresenius Environ. Bull.* **2011**, *20*, 773−778.

(63) (a) Becke, A. D. Density-Functional Thermochemistry. 3. The role of exact exchange. *J. Chem. Phys.* **1993**, *98*, 5648−5652. (b) Lee, C. T.; Yang, W. T.; Parr, R. G. Development of the colle-salvetti correlation-energy formula into a functional of the electron-density. *Phys. Rev. B* **1988**, *37*, 785−789.